Investigation into crystal structure-dielectric property correlation in barium titanate nanocrystals of different sizes

Journal:	*Nanoscale*
Manuscript ID	NR-ART-01-2023-000350.R1
Article Type:	Paper
Date Submitted by the Author:	16-Mar-2023
Complete List of Authors:	Li, Qiong; Case Western Reserve University, Macromolecular Science and Engineering Ju, tianxiong; Case Western Reserve University, Macromolecular Science and Engineering Li, Ruipeng; Brookhaven National Laboratory, Condensed Matter Physics and Materials Science Department Wang, Shuang; Hebei University of Technology, Yang, Yongfang; Hebei University of Technology, Ishida, Hatsuo; Case Western Reserve University, Macromolecular Science and Engineering Harn, Yeu-Wei; Georgia Institute of Technology, Materials Science and Engineering Chen, Jihua; Oak Ridge National Laboratory, Center for Nanophase Materials Sciences Hirt, Benjamin; Case Western Reserve University, Materials Science and Engineering Sehirlioglu, Alp; Case Western Reserve University, Materials Science and Engineering Lin, Zhiqun; National University of Singapore, Chemical and Biomolecular Engineering Zhu, Lei; Case Western Reserve University, Macromolecular Science and Engineering

Investigation into crystal structure-dielectric property correlation in barium titanate nanocrystals of different sizes †

Qiong Li [1], Tianxiong Ju [1], Ruipeng Li [2], Shuang Wang [3], Yongfang Yang [3], Hatsuo Ishida [1],
Yeu-Wei Harn [4], Jihua Chen [5], Benjamin Hirt [6], Alp Sehirlioglu [6],
Zhiqun Lin [7,*], and Lei Zhu [1,*]

[1] Department of Macromolecular Science and Engineering, Case Western Reserve University,
Cleveland, Ohio 44106, United States
[2] National Synchrotron Light Source II, Brookhaven National Laboratory, Upton, New York
11973, United States
[3] Institute of Polymer Science and Engineering, Hebei Key Laboratory of Functional Polymers,
Hebei University of Technology, Tianjin 300130, P. R. China
[4] School of Materials Science and Engineering, Georgia Institute of Technology, Atlanta,
Georgia 30332, United States
[5] Center for Nanophase Materials Sciences, Oak Ridge National Laboratory, Oak Ridge,
Tennessee 37831, United States
[6] Department of Materials Science and Engineering, Case Western Reserve University,
Cleveland, Ohio 44106, United States
[7] Department of Chemical and Biomolecular Engineering, National University of Singapore,
Singapore 117585, Singapore

* Corresponding authors. Emails: lxz121@case.edu (L.Z.) and z.lin@nus.edu.sg (Z.L.)

† Electronic supplementary information (ESI) available. See DOI: https://doi.org/xxxxxxxxx

Abstract

For high capacitance multilayer ceramic capacitors, high dielectric constant and lead-free ceramic nanoparticles are highly desired. However, as the particle size decreases to a few tens of nanometers, their dielectric constant significantly decreases, and the underlying mechanism has yet to be fully elucidated. Herein, we report a systematic investigation into the crystal structure-dielectric property relationship of combustion-made $BaTiO_3$ (BTO) nanocrystals. When the nanocrystal size is 100 nm and below, metastable paraelectric cubic phase was found in as-received BTO (denoted as arBTO) nanocrystals based on X-ray diffraction (XRD) study. Stable ferroelectric tetragonal phase was present when the nanocrystal size is above 200 nm. Notably, the cubic arBTO (particle size ≤100 nm) exhibited tetragonal fluctuations as revealed by Raman spectroscopy, whereas the tetragonal arBTO (particle size ≥200 nm) contained ~10% cubic fraction according to the Rietveld fitting of the XRD profiles. Thermal annealing the multi-grain tetragonal arBTO at 950 °C yielded single crystals of annealed BTO (denoted as anBTO), whose dielectric constants became higher than those of arBTO. However, the single crystalline anBTO prevented the formation of 90° domains; therefore, they exhibited a low dielectric constant of ~300. Although X-ray photoelectron spectroscopy and high-resolution transmission electron microscopy could not identify the exact structural defects, our study revealed that surface and bulk defects formed during synthesis affect the final crystal structures and thus dielectric properties of BTO nanocrystals with different sizes. The understanding obtained from this study will help us design high dielectric constant perovskite nanocrystals for next-generation multilayer ceramic capacitor applications.

Keywords: $BaTiO_3$ nanocrystals, structural defects, dielectric constant, paraelectric, ferroelectric

Introduction

The fast development in modern power and electronic industries, such as electric vehicles, renewable energy generation, and portable/wearable electronics, creates urgent demands for novel nanodieletric materials with high energy density, high breakdown strength, and low loss. Lead-free barium titanate ($BaTiO_3$ or BTO) nanocrystals represent an important class of such nanodielectrics, and they find practical applications in multilayer ceramic capacitors.[1-4] To further miniaturize multilayer ceramic capacitors with a high capacitance density (i.e., individual dielectric layer thickness <500 nm), BTO nanocrystals should achieve nanometer sizes while maintaining high dielectric constants (high-κ).[3, 5] This, however, remains challenging as the dielectric constant substantially decreases as the particle size decreases,[6] signifying an important size effect. Namely, as the nanocrystal sizes decrease below 100 nm, the ferroelectric tetragonal phase largely disappears, and the paraelectric cubic BTO nanocrystals often dominate with a low dielectric constant of only ~100. Even for large ferroelectric BTO nanocrystals (e.g., ≥200 nm), the dielectric constant (a few hundred) is still significantly lower than the typical values (~5000) of bulk BTO ceramics.[6, 7]

The high dielectric constant of ferroelectric ceramics originates from the ionic and dipolar polarization within both the ferroelectric domains and domain walls.[8, 9] To achieve high dielectric constants, it is essential to utilize nanostructured ceramics with a pronounced domain/domain wall contribution. For polycrystalline bulk BTO, which is usually obtained by sintering nanocrystals above 1000 °C, the room-temperature dielectric constant shows a clear relationship with the grain size.[7, 9, 10] When the grain size decreases from tens of μm to ~1 μm, the dielectric constant has a sharp increase from 1800 to 5000. As the grain size further decreases, the dielectric constant drops to ~1000 for sintered $BaTiO_3$ with a grain size of 20-50 nm.[7] This observation is elucidated by different domain structures in the bulk ferroelectric ceramics. For tetragonal BTO, two types of ferroelectric domain boundaries exist, 180° and 90°. The 180° domain wall is formed between two crystal lattices with anti-parallel polarizations and identical strain states due to minimization of the electrostatic energy. The 90° domain wall forms due to minimization of the internal strain energy of close-packed grains, as the sample is cooled through the Curie temperature (T_C) into the ferroelectric phase. The 90° domains and domain walls contribute more significantly to the dielectric constant than their 180° counterparts mainly due to the transition through the cubic-like structure within the 90° domain wall and the associated structural instability.[8, 9] When the grain size decreases to ~1 μm, the 90° domains reach the highest population density, resulting in the maximum dielectric constant around 5000. As the crystal grains decreases below 1 μm, the 90° domains gradually disappear. Combining with the effect of grain boundaries, which have a low permittivity, the dielectric constant of bulk BTO drops with decreasing the grain size below 1 μm.[11]

For BTO nanocrystals, a different trend of dielectric constant as a function of particle size is seen, which is widely regarded as a "simple" size effect.[6] When the size of the tetragonal BTO nanocrystals decrease from ~100 μm to 2 μm, a decrease in dielectric constant from ~850 to ~200 is observed.[12, 13] Such a decrease can be ascribed to the gradual elimination of multiple crystalline grains in one BTO crystal, and thus there is no need to minimize the internal strain energy for multiple grains. As 90° domains largely disappear with decreasing grain boundaries, only 180° domains remain. Around 200 nm, the BTO nanocrystals become more or less single crystalline. When the size further decreases to 100 nm or below, the paraelectric cubic nanocrystals are obtained regardless of the synthesis methods,[14] including hydrothermal,[15] sol-gel,[16] combustion,[17] and solid-state reaction methods.[18] The dielectric constant of these cubic BTO nanocrystals is around 100.[16, 19-21] Recently, efforts have been made to enhance dielectric constants of small BTO nanocrystals. For example, using a star-like block copolymer nanoreactor approach, uniform BTO nanocrystals with the particle size of 10-30 nm have been synthesized.[14, 22, 23] Unlike other BTO nanocrystals, these small BTO nanocrystals exhibit mixed ferroelectric phases at room temperature and thus had a relatively high dielectric constant in the range of 300-550, highlighting the need to consider other factors as build-in defects beyond the simple size effect.

In this work, a set of commercial BTO nanocrystals (50-500 nm) made by the combustion method are chosen to unravel the crystal structure-dielectric property relationship. To reduce the structural defects, these BTO nanocrystals are thermally annealed at 950 °C for 72 h, and the changes in dielectric properties are used to elucidate effects of structural defects in BTO nanocrystals.

Experimental

Materials

BTO nanocrystals (99.9% and average particle size from 50 to 500 nm) were purchased from U.S. Research Nanomaterials, Inc. (Houston, TX). The samples are named as arBTOx, where x is the particle size in nanometers. EcoflecxTM 00-30 silicone rubber was purchased from Smooth-on, Inc. Multidomain $BaTiO_3$ single crystal (BTO SC) with (001) orientation (5 mm × 5 mm × 0.5 mm, both sides polished) was purchased from MSE Supplies, LLC (Tucson, AZ). Ethanol, chloroform, and all other solvents were purchased from Fisher Scientific (Waltham, MA) and used without purification.

For thermal annealing, the arBTO powders were placed in a 10 mL alumina crucible and heated in a high-temperature box furnace (SentroTech, Strongsville, OH) under ambient pressure to different temperatures (800, 850, 900, and 950 °C) for up to 72 h to reduce structural defects. The samples with thermal annealing at 950 °C are denoted as anBTOx, where x is the as-received particle size in nanometers.

Characterization methods and instrumentation

Thermo Fisher Apreo 2 field-emission scanning electron microscope (SEM), operating at 10 kV and 0.1 nA, was used to examine the particle sizes and distribution before and after thermal annealing of BTO nanocrystals. Attenuated total reflection Fourier transform infrared (FTIR) spectroscopy experiments were performed using an Agilent Cary 630 FTIR spectrometer (Agilent Technologies, Santa Clara, CA) with a single-reflection diamond crystal. The FTIR spectra were collected under the ambient condition from 4000 to 400 cm^{-1} with 32 scans and 4 cm^{-1} resolution. A deuterated triglycine sulfate detector was used.

Differential scanning calorimetry (DSC) was performed using a TA Discovery DSC250 (TA Instruments, New Castle, DE) at a scanning rate of 10 °C/min under a dry nitrogen atmosphere (flow rate of 50 mL/min). Approximately, 10 mg of powder samples were sealed in an aluminum pan for each measurement. High-temperature DSC was performed using a 404 F1 Pegasus® DSC (Netzsch, Selb, Germany) at a scanning rate of 10 °C/min up to 1400 °C under an argon atmosphere (flow rate of 40 mL/min). Approximately, 20 mg of powder samples were placed in an alumina crucible with a cap for each measurement.

Powder X-ray diffraction (XRD) experiment was performed in the reflection mode at room temperature using a Rigaku SmartLab X-ray diffractometer equipped with a sealed X-ray tube operating at 40 kV and 30 mA. The X-ray source contained 2 wavelengths: 0.15406 nm for Cu $K_{\alpha 1}$ and 1.5444 Å for Cu $K_{\alpha 2}$ with intensity ratio close to 2:1. A HyPix-3000 area detector was used to collect the data. SmartLab Studio II software was used for the Rietveld refinement analysis. Temperature-dependent 2D WAXD patterns were collected at the 11-BM Complex Material Scattering (CMS) beamline of the National Synchrotron Light Source II (NSLS-II), Brookhaven National Laboratory. The monochromatized X-ray wavelength was $\lambda = 0.0729$ nm. Each WAXD pattern was acquired for 10 s with a Pilatus 800K (Dectris, Baden, Switzerland) detector, and the sample to detector distance was calibrated using silver behenate as 259 mm [the first-order reflection at a scattering vector of $q = (4\pi\sin\theta)/\lambda = 1.076$ nm]. One-dimensional (1D) WAXD curves were obtained by integrating the corresponding 2D WAXD patterns radially using the xPolar software developed by Stonybrook Technology and Applied Research, Inc.

A back-scattering Raman spectrometer (XploRA, Horiba, Kyoto, Japan) was used with a helium-neon laser (785 nm) excitation. Measurements were performed on hydraulically compressed (148 MPa) BTO disks (without any additives) in the range from 100 to 1000 cm^{-1} with a 20× objective lens, a 200 nm slit width, a 1200 lines/mm grating, and 10% laser power. Each spectrum was obtained by averaging 15 scans of a 5-s acquisition. Temperature-dependent Raman measurements were carried out during stepwise cooling from 250 to 50 °C, using a HCS402 heating stage (Instec, Inc., Boulder, CO) for the compressed BTO disks. The actual temperature at the top surfaces of the pressed BTO disks were calibrated using a digital infrared thermometer.

X-ray photoelectron spectroscopy (XPS) measurement was carried out using a PHI 5000 VersaProbe XPS Microprobe (Physical Electronics, Inc., Chanhassen, MN) with a monochromated Al Kα X-ray source (1486.6 eV) and a hemispherical analyzer. The X-ray beam spot size was 200 μm and the energy resolution was 0.68 eV full-width at half- maximum. The high-resolution scans were carried out on Ba $3d_5$ for 6 scans and on Ti 2p for 18 scans. Carbon 1s peak position of two high-resolution scans was used for calibration.

Field-emission scanning transmission electron microscope (TEM) was performed on an FEI Tecnai G2 F20 (FEI Company, Hillsboro, Oregon). Atomic-resolution high-angle annular dark-field imaging (HAADF) was performed on a probe-corrected FEI Themis-Z^{TM} at the Center for Electron Microscopy and Analysis (CEMAS), Ohio State University. TEM samples were prepared as the following. The arBTO50 powder was dispersed in ethanol under ultrasonication, followed by drop-cast onto a copper TEM grid having an ultra-thin carbon (< 3 nm) on a lacey carbon support film (Ted Pella, Redding, CA) for direct observation. The arBTO200 and anBTO200 powders were dispersed in ethanol under ultrasonication and drop-cast onto a conductive silicon wafer substrate to form a monolayer. The wafer substrate was transferred into a focused ion beam (FIB)-SEM (FEI Nova Nano SEM 450) for TEM sample preparation. A thin platinum layer (~200 nm) was firstly deposited by electron beam to fix the BTO nanocrystals on the silicon wafer, and another platinum layer (~800 nm) was deposited by ion beam to protect the top surface from the ion beam trimming in the next step. Then, an in-situ “lift-out” technique was carried out to cut free a section of approximate 10 µm × 5 µm × 2 µm material containing the region of interest and welded on a TEM grid by transferring with the Omniprobe. Finally, the attached sample foil was thinned by ion beam to a thickness so that it could be suitable for high-resolution TEM imaging. To remove the amorphous surface layers caused by FIB, additional milling was performed on the thinned TEM samples using a FEI Helios 600 NanoLab FIB/SEM with 30 kV Ga ion beam at 100 pA.

Broadband dielectric spectroscopy (BDS) was performed on a Novocontrol Concept 80 broadband dielectric spectrometer (Novocontrol Technologies, Montabaur, Germany) with a liquid nitrogen temperature control system. The applied voltage was 1 V_{rms} (root-mean square voltage) with frequency ranging from 1 Hz to 1 MHz and temperature ranging from -40 to 180 °C.

To measure the permittivity of BTO nanocrystals, BTO powders were mixed with silicone rubber at an 80/20 volume ratio using chloroform as the solvent. After evaporation of chloroform, the BTO-rubber mixture was heated at 80 °C in a vacuum oven overnight to allow the silicone rubber to fully cure. Then, the BTO-rubber composites were isostatically pressed with a hydraulic press at 148 MPa with a 13 mm die to prepare a cylindrical pellet (about 0.4 mm thick). Gold (Au) electrodes (ca. 10 nm) were evaporated on both sides of the pressed pellet using a Quorum Q300T D Plus sputter coater (Quorum Technologies, Laughton, East Sussex, UK). The electrode area was 78.5 mm^2. To measure the permittivity of the BTO (001)-SC, Au electrodes with an area of 7.06 mm^2 were evaporated on both surfaces of the disk sample.

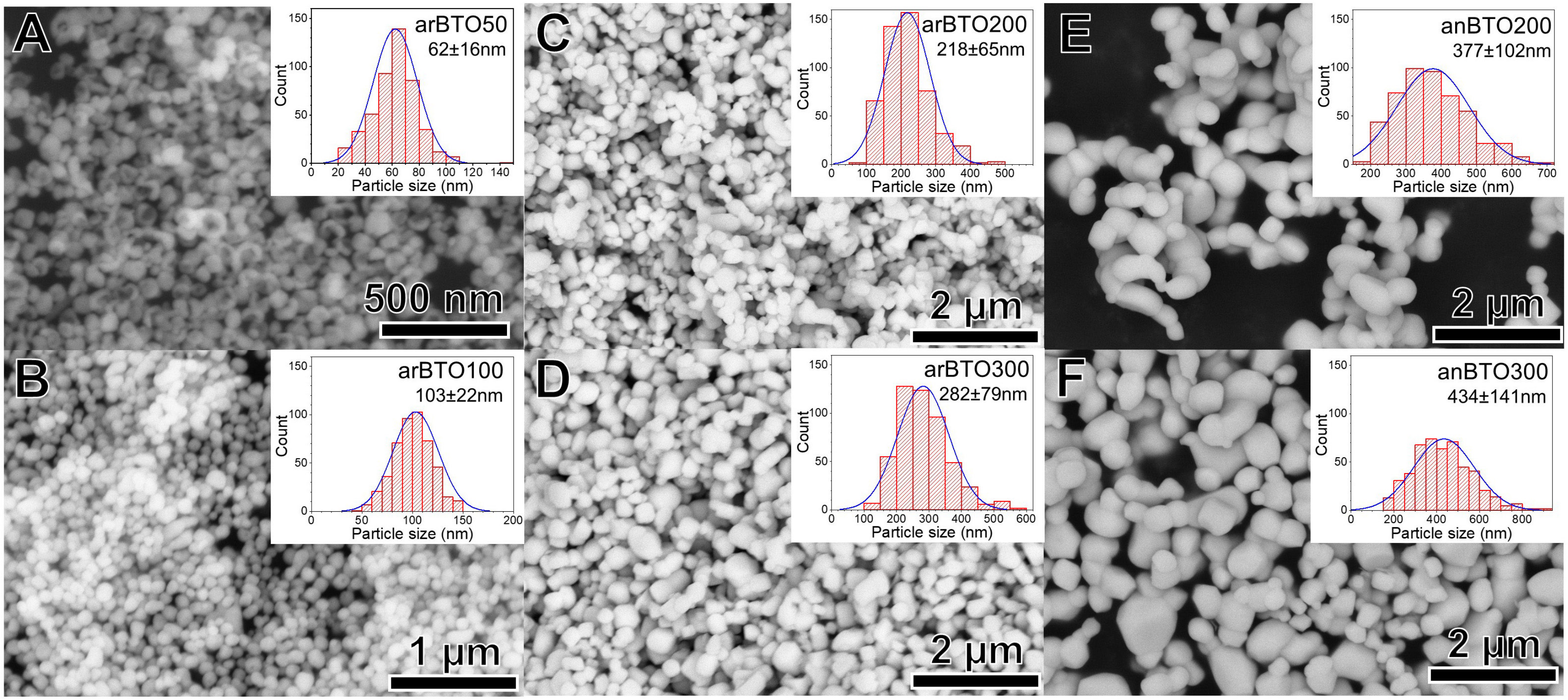

Fig. 1. SEM micrographs of (A) arBTO50, (B) arBTO100, (C) arBTO200, (D) arBTO300, (E) anBTO200, and (F) anBTO300. The insets show particle-size histograms and the mean particle size with error (i.e., mean ± standard deviation).

Results and discussion

Particle size analysis and thermal annealing to improve crystalline structure for BTO nanocrystals

According to the vendor data, the purity of BTO nanocrystals was 99.9%. In addition, FTIR spectroscopy was used to confirm the purity of all arBTO samples (see Fig. S1 in the Supporting Information). A strong Ti-O vibrational band at 486 cm^{-1} and a characteristic Ba-Ti-O peak at 1450 cm^{-1} corresponded to crystalline BTO.[24] There were no obvious impurity absorption bands except for the single-bounce diamond crystal absorption at 1900-2240 cm^{-1} and CO_2 peaks around 2346 cm^{-1}. No lattice hydroxyl defects[25] were found in these combustion-made BTO powders.

SEM micrographs of arBTO50, arBTO100, arBTO200, and arBTO300 nanocrystals are shown in Figs. 1A-D, and those of arBTO400 and arBTO500 are shown in Figs. S2A,C, respectively. The insets show the particle size histograms obtained by manually counting over 500 particles for each sample. The arBTO50 nanocrystals had a donut-shaped morphology with an average size of 62 ± 16 nm (i.e., mean ± standard deviation), possibly due to the low-concentration precursor in the combustion synthesis. The arBTO100, arBTO200, arBTO300, arBTO400, and arBTO500 nanocrystals were roughly spherical in shape with average sizes of 103 ± 22, 218 ± 65, 282 ± 79, 393 ± 120, and 473 ± 130 nm, respectively (Table 1).

Table 1. Characterization data for arBTO and anBTO nanocrystals.

Sample	Size by SEM (nm)	Crystallite size, D (nm) [a]	Microstrain, ε ($\times 10^{-4}$) [a]	Phases [b]	ΔH_C (J/g)	ε_r at 1 kHz and 25 °C [c]
arBTO50	62±16	43	29.3	97.80(7)% cubic 2.20(7)% $BaCO_3$	0	87
arBTO100	103±22	85	25.5	98.33(8)% cubic 1.67(8)% $BaCO_3$	0	94
arBTO200	218±65	99	1.21	85.67(8)% tetragonal 12.82(3)% cubic 1.52(9)% $BaCO_3$	0.550	105
arBTO300	282±79	132	2.26	86.0(4)% tetragonal 13.1(4)% cubic 0.84(7)% $BaCO_3$	0.537	102
arBTO400	393±120	152	2.26	89.0(3)% tetragonal 11.0(3)% cubic	0.637	96
arBTO500	473±130	163	1.25	90.6(4)% tetragonal 9.4(4)% cubic	0.753	97
anBTO200	377±102	140	2.25	87.5(2)% tetragonal 12.5(2)% cubic	0.821	300
anBTO300	434±141	142	2.68	87.3(3)% tetragonal 12.7(3)% cubic	0.859	220
anBTO400	508±145	166	2.25	89.8(3)% tetragonal 10.2(3)% cubic	0.918	170
anBTO500	567±155	195	2.17	92.3(3)% tetragonal 7.7(3)% cubic	1.045	149

[a] Calculated by the Williamson-Hall equation,[26] using full-width at half maximum (β, in radians) of different reflections: $\beta cos\theta = K\lambda/D + 4\varepsilon sin\theta$, where θ is the half scattering angle, K is a dimensionless shape factor (~0.94), λ is the $K_{\alpha 1}$ wavelength, D is the crystallite size, and ε is the microstrain.

[b] Obtained by the Rietveld fitting (see Figs. S7 and S8).

[c] After correction with the Bruggeman mixing rule. Errors in ε_r primarily come from the pellet thickness and packing density variations, which is about 10%.

According to a previous report using the Williamson-Hall powder XRD analysis,[26] thermal annealing at elevated temperatures decreased the microstrain of the crystal lattice. This suggested that crystalline grains and ferroelectric domains can be improved by reducing structural defects via thermal annealing. To further improve the crystalline structure and reduce defects in arBTO nanocrystals, thermal annealing at elevated temperatures was performed. High-temperature and conventional DSC and SEM were employed to determine the optimal thermal annealing temperature, which should be as high as possible without significant particle-sintering, i.e., nanocrystals merging into micron-sized or larger particles without liquefaction. For this purpose, arBTO50, arBTO100, and arBTO200 nanocrystals were studied. High-temperature DSC in Fig. S3A shows that all the arBTO nanocrystals started the major melting process when heated beyond 1000 °C. The arBTO50 had an obvious pre-melting peak around 800 °C due to defects in the small particles. The arBTO100 had a weak pre-melting peak around 708 °C. The arBTO200 did not show any pre-melting peak. Therefore, we chose 800-950 °C for the thermal annealing study and the annealing time was chosen as 72 h. Conventional DSC was performed for thermally annealed arBTO100 and arBTO200, as shown in Figs. S3B,C. For the paraelectric arBTO100 (which did not show any sharp transitions up to 150 °C), a weak Curie transition was observed at 128 °C with the heat of Curie transition (ΔH_C) being 0.22 J/g for the sample annealed at 800 °C. With increasing the thermal annealing temperature, the Curie transition became more obvious with ΔH_C increased to 0.90 J/g for the sample annealed at 950 °C. Fig. S4 shows SEM micrographs of arBTO100 annealed at 800-950 °C. The high magnification micrographs (the top panel of Fig. S4) showed that the particle size increased to 171 ± 50, 254 ± 76, 259 ± 71 nm, and 462 ± 130 nm for the annealing temperatures of 800, 850, 900, and 950 °C, respectively, because of the Ostwald ripening (i.e., small particles gradually melt, and the material deposits onto large particles to increase their sizes).[27] Meanwhile, large porous ball-shaped clusters were observed at low magnifications (the lower panel of Fig. S4) with small particles loosely sticking together. Upon mechanical crushing, these loose clusters could be easily broken up into individual particles (e.g., see Fig. S4F). This observation suggested that the pre-melting should have involved surface-melting of particles followed by the Ostwald ripening process. For the ferroelectric arBTO200, the Curie transition temperature (T_C) was observed around 130 °C and the ΔH_C gradually increased to 0.82 J/g after annealing at 950 °C (Fig. S3C). Similar to thermally annealed arBTO100, individual particle size gradually increased from 218 ± 65 nm for arBTO200 to 356 ± 101 nm for the sample annealed at 900 °C due to the Ostwald ripening (see the top panel high-magnification micrographs in Fig. S5). However, particle clustering was not observed until 850 °C and the degree of clustering was much less than that of arBTO100; see the bottom panel low-magnification micrographs in Fig. S5.

From the above study, 950 °C was chosen as the thermal annealing temperature for arBTO nanocrystals because it was high enough to effectively reduce defects in nanocrystals, but at the same time was still below the onset temperature (1000 °C) of sintering (see Fig. S3A). However, annealing arBTO50 and arBTO100 at 950 °C for 72 h led to significant particle-sintering. As shown in SEM micrographs in Figs. S4H (950 °C-annealed arBTO100, or anBTO100) and S6 (950 °C-annealed arBTO50, or anBTO50), close to micron-sized particles were often observed. It is not possible to remove these sintered particles from the ripened nanocrystals; therefore, we will exclude anBTO50 and anBTO100 from further study. On the contrary, no obvious particle-sintering was observed for anBTO200-anBTO500.

The SEM micrographs for thermally annealed (at 950 °C for 72 h) anBTO200 and anBTO300 are displayed in Figs. 1E,F, and those for anBTO400 and BTO500 are presented in Figs. S2B,D, respectively. Compared with arBTO nanocrystals, the anBTO nanocrystals significantly ripened: the average sizes for anBTO200, anBTO300, anBTO400, and anBTO500 increased to 377 ± 102, 434 ± 141, 508 ± 145, and 567 ± 155 nm, respectively (Table 1). Note that the arBTO nanocrystals were prepared by the high-temperature combustion method; therefore, they should not contain any amorphous fractions (see powder XRD and TEM results later). Thermal annealing did not make the nanocrystals more crystalline, but less defective together with Ostwald ripening.

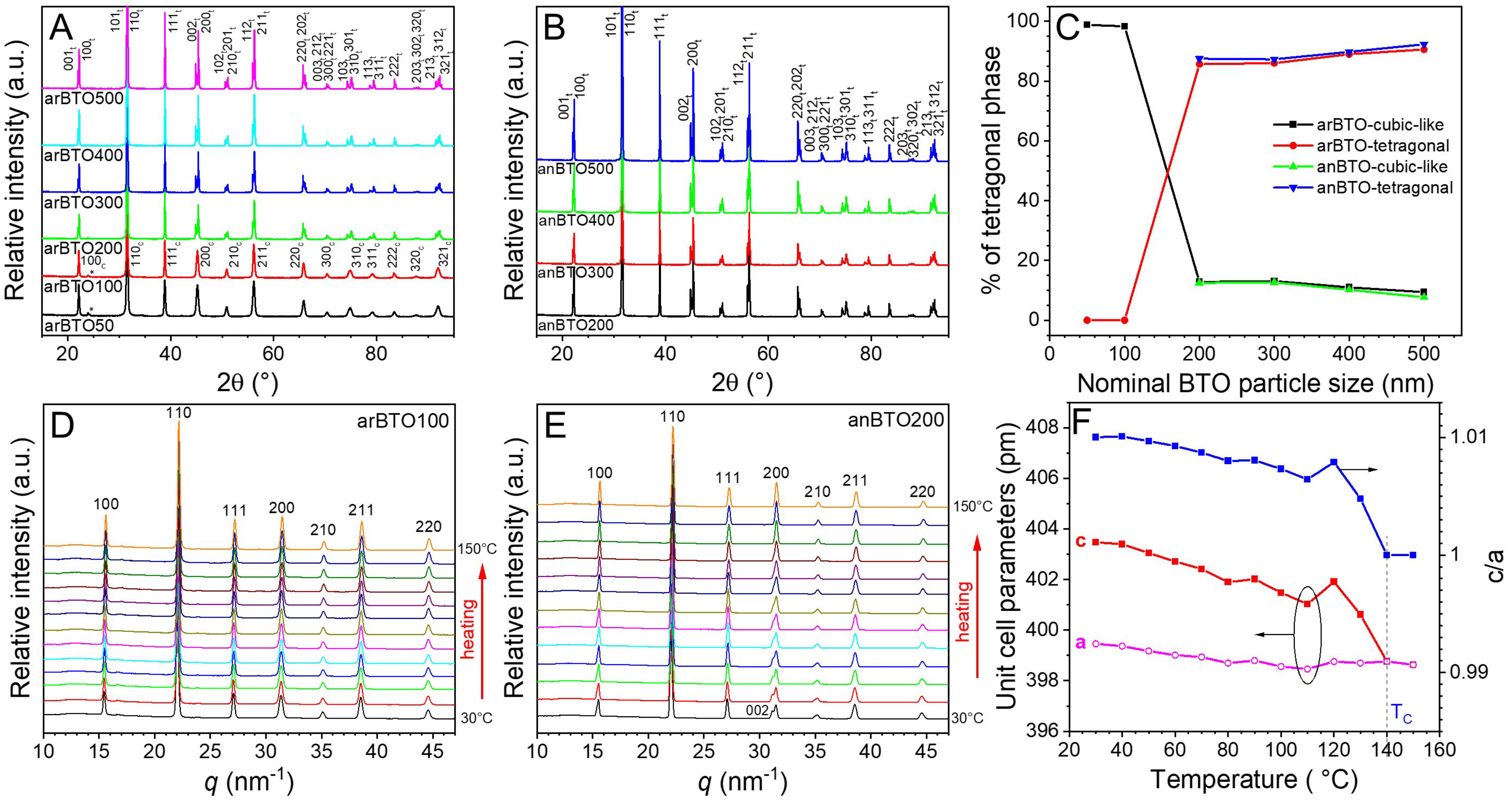

Fig. 2. Powder XRD profiles of (A) arBTO50-arBTO500 and (B) anBTO200-anBTO500 at room temperature. (C) shows the corresponding contents of the tetragonal phase and the cubic-like fraction versus the nominal BTO nanocrystal size, obtained from the Rietveld fitting. Temperature-dependent XRD for (D) arBTO100 and (E) anBTO200 with (F) the unit cell parameters and the *c*/*a* ratio for anBTO200 at different temperatures during a stepwise heating and cooling cycle.

Crystal structures of arBTO and anBTO nanocrystals studied by XRD and Raman spectroscopy

The crystal structures of arBTO and anBTO nanocrystals were first studied by XRD. Figs. 2A and 2B show reflection powder XRD profiles of arBTO and anBTO nanocrystals at room temperature, respectively. To determine the polymorphism, these powder XRD profiles were fitted with the Rietveld method using the SmartLab Studio II software; see Fig. S7 for arBTO and Fig. S8 for anBTO. For arBTO50 and arBTO100 (Fig S7), a pure cubic phase was identified, together with a small percentage of witherite $BaCO_3$ impurity (~2 wt.%). It was likely that the combustion process in the air produced some $BaCO_3$ impurity in the arBTO nanocrystals. For arBTO200-arBTO500 (Fig. S7), both tetragonal and cubic $BaTiO_3$ phases were identified with the tetragonal phase being the major component. Again, a small fraction of witherite $BaCO_3$ was observed as well. For anBTO200-anBTO500 (Fig. S8), the witherite $BaCO_3$ largely disappeared because of the thermal decomposition during annealing at 950 °C for 72 h. Again, the major tetragonal phase was identified, together with a minor cubic phase. However, the intensity of individual XRD peaks substantially increased and the peak width slightly decreased for anBTO nanocrystals, indicating growth of the crystalline grains after 950 °C annealing. Detailed Rietveld fitting results of the first 6 reflections for arBTO and anBTO nanocrystals are shown in Figs. S9 and S10, respectively. Fig. 2C and Table 1 summarizes the contents of the tetragonal and cubic phases for arBTO and anBTO nanocrystals. As we can see, after thermal annealing at 950 °C, the tetragonal content in anBTO slightly increased as compared to arBTO (about 2%).

The coexistence of tetragonal and cubic phases in sintered $BaTiO_3$ [28] and nanocrystalline $BaTiO_3$ [29-31] has been reported before. Especially for $BaTiO_3$ nanocrystals, both bulk and surface defects can induce the metastable cubic phase even below the Curie temperature (i.e., 120 °C for sintered $BaTiO_3$). For $BaTiO_3$, the cubic fraction may exist in the ferroelastic domain walls and can be related to microstrain at these walls.[32] For $BaTiO_3$ nanocrystals, it is often considered that the cubic component exists in the outer layer of the particle and the inner core is tetragonal.[31] It is also possible that between the inner tetragonal core and the outer cubic shell, there exists a transition zone with the crystal unit cells gradually transforming from tetragonal to cubic.[30] According to ref. 28, when the $BaTiO_3$ nanocrystal size becomes too small, the inner tetragonal core largely disappear and the nanocrystal will be in the defect-induced cubic phase.

The Williamson-Hall plot was used to analyze the crystallite size (D) and the inhomogeneous stain or microstrain (ε) of the crystallite:[33]

$$\beta cos\theta = \frac{K\lambda}{D} + 4\varepsilon sin\theta \tag{1}$$

where β is the full-width at half maximum (in radians), θ is the half scattering angle, K is a dimensionless shape factor (~0.94), and λ is the $K_{\alpha 1}$ wavelength. The plots for various BTO nanocrystals are shown in Fig. S11, and the results are presented in Table 1. After 950 °C annealing, the crystallite size increased for the anBTO samples, as compared to the arBTO samples. Meanwhile, the cubic arBTO50 and arBTO100 exhibited microstrain values (25.5-29.3 $\times 10^{-4}$) about 10 times higher than those (1.21-2.68 $\times 10^{-4}$, which is similar to the literature value for tetragonal BTO bulk sample[34]) of the tetragonal arBTO and anBTO samples. Note that microstrain can be caused by dislocations, vacancies, grain boundaries, and residue stresses that cause a nonuniform distortion of the crystal lattice. Therefore, the higher microstrain values for arBTO50 and arBTO100 indicated more structural defects in the cubic nanocrystals.

Temperature-dependent XRD was performed for arBTO100 and anBTO200, and results are shown in Figs. 2D,E. For arBTO100, no apparent change in the cubic phase was observed during the heating and cooling cycle between 30 and 150 °C (Fig. 2D), and the unit cell parameter changed monotonically (see Fig. S12). For the tetragonal anBTO200, the split $(200)_t$ and $(002)_t$ merged together at 140 °C upon heating, and the peak-splitting reappeared at 130 °C upon cooling (Fig. 2E), indicating the reversible Curie transition. The tetragonality, defined by c/a, slightly decreased from 1.01 at 30 °C with increasing the temperature, and finally dropped to 1.00 at 140 °C upon heating, featuring the Curie transition (Fig. 2E). Additional temperature dependent XRD experiments were carried out for other arBTO (Fig. S13) and anBTO samples (Fig. S14), and similar phenomena were observed.

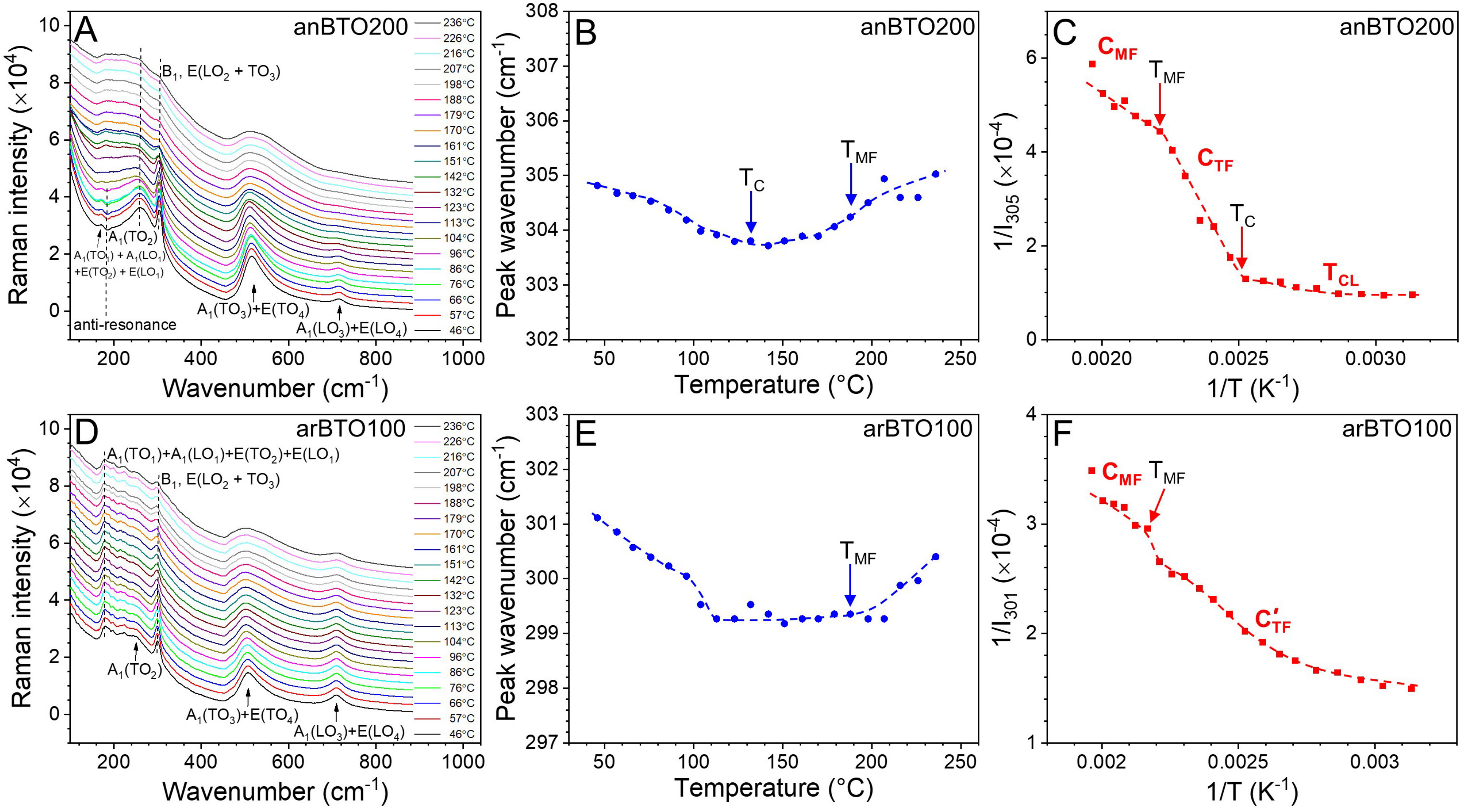

Fig. 3. Temperature-dependent Raman spectra of (A) anBTO200 with (B) the 305 cm^{-1} peak position and (C) 1/I$_{305}$ versus 1/T. Temperature-dependent Raman spectra of (D) arBTO100 with (E) the 301 cm^{-1} peak position and (F) 1/I$_{305}$ versus 1/T. Peak assignments are given in (A) and (D).

While XRD detects the global (or average) crystal structure, Raman detects much localized structures at the bonding level. The room temperature Raman spectra of different arBTO samples are shown in Fig. S15A. The Raman peak intensities increased with the particle size, but were not linearly proportional (Fig. S15B). There was a stepwise increase in the peak intensities when arBTO transitioned from the cubic phase (particle size ≤100 nm) to the tetragonal phase (particle size ≥200 nm). This result is consistent with the literature report,[35] and could be attributed to both effects of crystal structure and particle size.

To understand the detailed structures of both cubic and tetragonal BTO nanocrystals, temperature-dependent Raman study was performed for anBTO200 (tetragonal) and arBTO100 (cubic). Results are shown in Fig. 3A,D, respectively. For anBTO200, typical tetragonal-active optical modes were observed at room temperature (Fig. 3A): $A_1(TO_1)+A_1(LO_1)+E(TO_2)+E(LO_1)$ at 171 cm^{-1}, $A_1(TO_2)$ at 260 cm^{-1}, $B_1+E(LO_2+TO_3)$ at 305 cm^{-1}, $A_1(TO_3)+E(TO_4)$ at 515 cm^{-1}, and $A_1(LO_3)+E(LO_4)$ at 715 cm^{-1}. Their assignments have been reported before.[36] Upon heating, the 305 cm^{-1} peak position gradually decreased, and reached a minimum value at 140 °C, above which the peak position gradually increased (Fig. 3B). When we plot the reciprocal peak intensity at 305 cm^{-1}, $1/I_{305}$, versus the reciprocal temperature, 1/T, two transitions could be identified in Fig. 3C. The first one was the Curie transition at 130 °C, below which anBTO200 exhibited the cubic-fluctuated tetragonal (T_{CF}) phase (as identified by XRD above) and $1/I_{305}$ remained low. Above T_C, where anBTO200 should become a neat cubic phase, $1/I_{305}$ largely increased. Theoretically, the neat cubic perovskite lattice should not show any active optical Raman modes, although experimentally the paraelectric $BaTiO_3$ exhibited two broad absorption bands around 260 and 515 cm^{-1}.[37, 38] The persistence of the 305 cm^{-1} peak above T_C for anBTO200 indicated that the paraelectric cubic phase must contain dynamic tetragonal-fluctuations (i.e., ergodic polar nanoregions[25, 39]) in the crystals. This tetragonal-fluctuated cubic phase is abbreviated as the C_{TF} phase. Similar C_{TF} phase was also reported before for both bulk and nanocrystal $BaTiO_3$ above T_C.[25, 40] Note that this tetragonal fluctuation should happen at a length scale of one or a few unit cells, much smaller than that of the nanodomains for relaxor ferroelectrics (i.e., at least several nanometers).[41, 42] Meanwhile, the C_{TF} phase in $BaTiO_3$ is different from the genuine paraelectric phase of $SrTiO_3$ at room temperature, which does not exhibit any sharp tetragonal absorption band around 305 cm^{-1}.[43] Given this feature, the Curie transition of $BaTiO_3$ was similar to the order-to-disorder transition observed in block copolymers.[44, 45] Above 190 °C, the 305 cm^{-1} peak became increasingly weaker (Fig. 3A), and a slope change was identified in the $1/I_{305}$ - $1/T$ curve in Fig. 3C. We consider that above 190 °C the tetragonal fluctuation substantially weakened, and the sample entered a mean-field cubic phase (C_{MF}). The transition temperature could be identified as the mean-field temperature (T_{MF}).

The cubic arBTO100 exhibited strong tetragonal-active Raman absorption bands at room temperature, suggesting again local tetragonal fluctuations in the global cubic phase (Fig. 3D). However, this cubic phase should be different from the dynamic C_{TF} phase for BTO above T_C (see Fig. 3A), because the tetragonal-active Raman bands were much stronger. We consider that the tetragonal fluctuations could be more static (i.e., non-ergodic) and the polar nanoregions should be larger than those in the C_{TF} phase above T_C. Therefore, this cubic phase of arBTO100 was assigned as the C'_{TF} phase. However, the concentration of these tetragonal fluctuations must be so low that no tetragonal reflections could be detected by XRD for arBTO100. For BTO nanocrystals prepared by different synthetic methods (hydrothermal, sol-gel, combustion, etc.),[14] the fraction of tetragonal fluctuations and the size of polar nanoregions may vary, depending on the defects (e.g., grain boundaries, vacancies, and surface layer) involved in the final products. As the fraction of tetragonal fluctuations and the size of polar nanoregions increased, the broad $(200)_c$ reflection would become increasingly split into two peaks. This is exactly observed experimentally in many literature reports.[21, 29, 46] Upon increasing temperature, the B_1+E(LO_2+TO_3) peak position gradually decreased from 301 cm^{-1} at room temperature and had a stepwise drop around 100 °C (Fig. 3E). Above 190 °C, the peak position slightly increased again. Fig. 3F shows $1/I_{301}$ versus 1/T for arBTO100, where $1/I_{301}$ gradually increased with an increase in temperature. No Curie transition was observed. Around T_{MF} at 190 °C, there was a step change in $1/I_{301}$, suggesting that the C'_{TF} phase entered the C_{MF} phase.

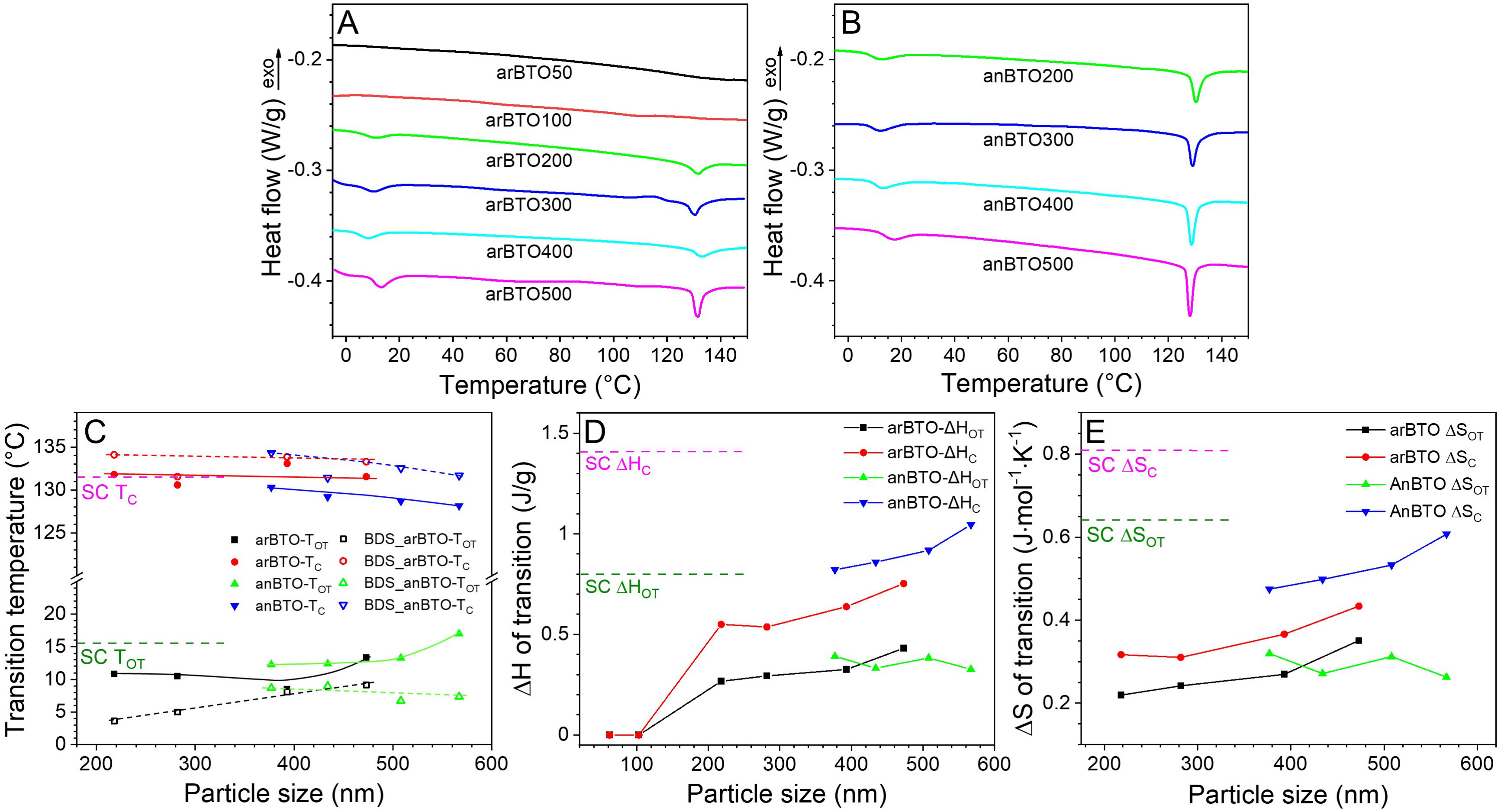

Fig. 4. Heating DSC curves of (A) arBTO50-arBTO500 and (B) anBTO200-anBTO500 nanocrystals with (C) phase transition temperatures, (D) heats of transition (ΔH) and (E) entropy changes of transition (ΔS) as a function of the actual particle size.

Thermal properties

Given the complex crystalline structures in arBTO and anBTO nanocrystals, their thermal properties should be largely affected. Comparing the DSC heating curves of arBTO in Fig. 4A and anBTO in Fig. 4B, the effect of thermal annealing on ferroelectric transitions could be clearly seen. First, arBTO50 and arBTO100 did not exhibit any sharp phase transition during the heating process, except for a very weak/broad endothermic peak around 140 °C. Note, all samples had been stringently dried to remove moisture; therefore, the effect from absorbed moisture was eliminated in this study. This is consistent with their C'_{TF} structure. For the rest arBTO samples, two ferroelectric transitions were seen: one around 11 °C for the orthorhombic-to-tetragonal (OT) transition and the other around 132 °C for the tetragonal-to-cubic (or Curie) transition (Fig. 4C). Note that the OT transition temperature (T_{OT}) was lower than that of BTO (001)-SC (~15 °C), whereas the T_C was similar to that of BTO (001)-SC (131.5 °C); see Fig. S16. The heats of transition were obtained by peak integration, and results are plotted in Fig. 4D. The heats of the OT transition (ΔH_{OT}) for arBTO nanocrystals increased from 0.27 J/g for arBTO200 to 0.29 J/g for arBTO300, 0.33 J/g for arBTO400, and 0.43 J/g for arBTO500, respectively. However, they were significantly lower than that of BTO (001)-SC (~0.80 J/g); see Fig. S16. The ΔH_C for arBTO nanocrystals changed from 0.55 J/g for arBTO200 to 0.54 J/g for arBTO300, 0.64 J/g for arBTO400, and 0.75 J/g for arBTO500. Again, these values were significantly lower than that of BTO (001)-SC (~1.45 J/g); see Fig. S16. The above results suggested larger ferroelectric domains for larger particles. Using $\Delta H_C = T_C \Delta S_C$, ΔS_C could be determined, as shown in Fig. 4E. For the BTO (001)-SC, $\Delta H_C = 1.46$ J/g (Fig. S16), and thus ΔS_C was calculated to be 0.81 J/(mol·K). It is clearly seen that ΔS_C values of arBTO and anBTO nanocrystals were smaller than that of BTO

(001)-SC (Fig. 4E), suggesting both arBTO and anBTO contained more defects than BTO (001)-SC.

After thermal annealing, T_{OT} slightly increased, and T_C slightly decreased for anBTO nanocrystals, as compared with those for arBTO nanocrystals (Figs. 4B,C). Intriguingly, all anBTO nanocrystals showed higher ΔH_C compared to their arBTO counterparts: 0.82 J/g for anBTO200, 0.86 J/g for anBTO300, 0.92 J/g for anBTO400, and 1.05 J/g for anBTO500 (Fig. 4D). The higher ΔH_C for anBTO nanocrystals could be attributed to larger ferroelectric domains after removal of crystalline defects by thermal annealing at 950 °C. Compared with BTO (001)-SC, anBTO nanocrystals still exhibited lower ΔH_C, suggesting that anBTO contained more defects. At last, their ΔH_{OT} and ΔS_{OT} for anBTO remained similar to those of arBTO, as seen in Figs. 4D,E.

The first cooling DSC curves for arBTO and anBTO nanocrystals are shown in Figs. S17A,B, respectively. The corresponding transition temperatures and heats of transition are summarized in Figs. S17C,D. Similar trends are observed for both transition temperatures and heats of transition, as discussed above for the heating curves, except for an undercooling (~5 °C) in the peak phase transition temperatures. This suggests that the Curie transition in these arBTO and anBTO nanocrystals was the first-order phase transition.

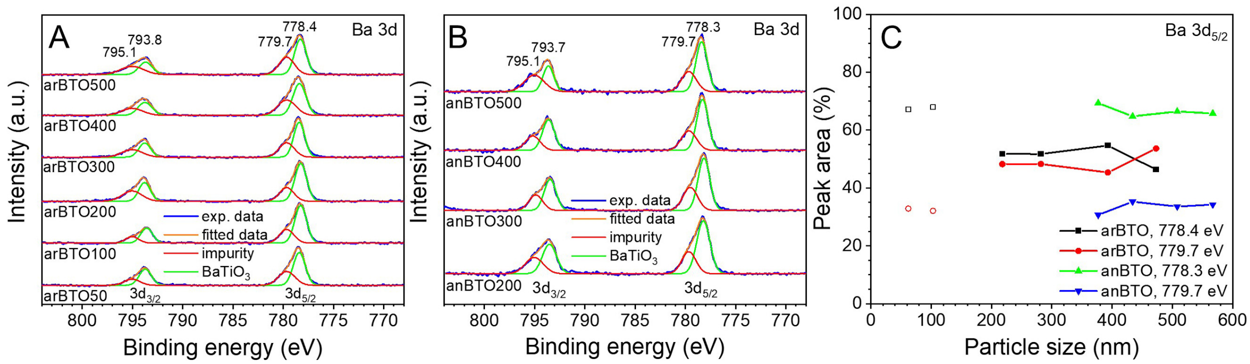

Fig. 5. Experimental XPS spectra of (A) arBTO50-arBTO500 and (B) anBTO200-anBTO500 nanocrystals with fitted percentage areas for (C) the Ba $3d_{5/2}$ peaks.

XPS study of surface defects

From the above XRD and Raman studies on macroscopic arBTO and anBTO samples, we consider that structural defects, rather than chemical defects such as hydroxyl groups, affect their thermal properties in DSC. These structural defects can be either surface or bulk defects, such as grain boundaries, domain walls, point defects, and dislocations. In the following, we attempt to study these defects using different experimental techniques. First, XPS was used to study surface defects and impurities, because the penetration depth for XPS is usually around 5 nm. Figs. 5A,B show the XPS spectra of arBTO and anBTO nanocrystals. In Fig. 5A, the high-resolution Ba 3d XPS spectra of arBTO had two major peaks at 793.8 and 778.4 eV, due to the splitting of the Ba $3d_{3/2}$ and Ba $3d_{5/2}$ spin states, respectively. For anBTO, these two peaks were slightly shifted to 793.7 eV and 778.3 eV. Meanwhile, shoulder peaks at 795.1 eV (Ba $3d_{3/2}$) and 779.7 eV (Ba $3d_{5/2}$) were seen for both arBTO and anBTO, indicating an impurity chemical state of Ba. Peak-fitting was used to calculate the percentage areas of the impurity phase and neat $BaTiO_3$. From the Ba $3d_{5/2}$ peak areas in Fig. 5C, the arBTO200-arBTO500 nanocrystals had a ~50% impurity phase, whereas the arBTO50 and arBTO100 had only 35% impurity. It is possible that the penetration depth for small and irregular shaped particles, such as arBTO50 and arBTO100, was higher and thus the percentage of impurity was lower. From the above XRD study with Rietveld fitting, a small fraction of witherite $BaCO_3$ was identified for arBTO nanocrystals. Therefore, it is likely that the impurity phase was witherite $BaCO_3$, which could form during the combustion synthesis (i.e., by reacting with CO_2 in air[47, 48]) and concentrate on the surface of arBTO nanocrystals. After thermal annealing at 950 °C, the shoulder Ba $3d_{5/2}$ peaks at 779.7 eV decreased in intensity. This may suggest thermal decomposition and thus decreased $BaCO_3$ impurity for anBTO (see Fig. 5C), and is consistent with the earlier XRD results (i.e., the witherite $BaCO_3$ content substantially decreased for anBTO). The high-resolution Ti 2p XPS spectra of BTO nanocrystals are shown in Fig. S18. The two peaks at 457.9 and 463.7 eV were assigned to the splitting of the Ti $2p_{3/2}$ and Ti $2p_{1/2}$ spin states, respectively. No obvious shoulder peaks could be identified, suggesting that there was no Ti-containing impurity on the surface of BTO nanocrystals. Although we have identified the $BaCO_3$ impurity on the arBTO surface, it is still not conclusive if it caused the structural defects in $BaTiO_3$ nanocrystals. Meanwhile, XPS would not be able to differentiate the tetragonal phase from the cubic phase for $BaTiO_3$.

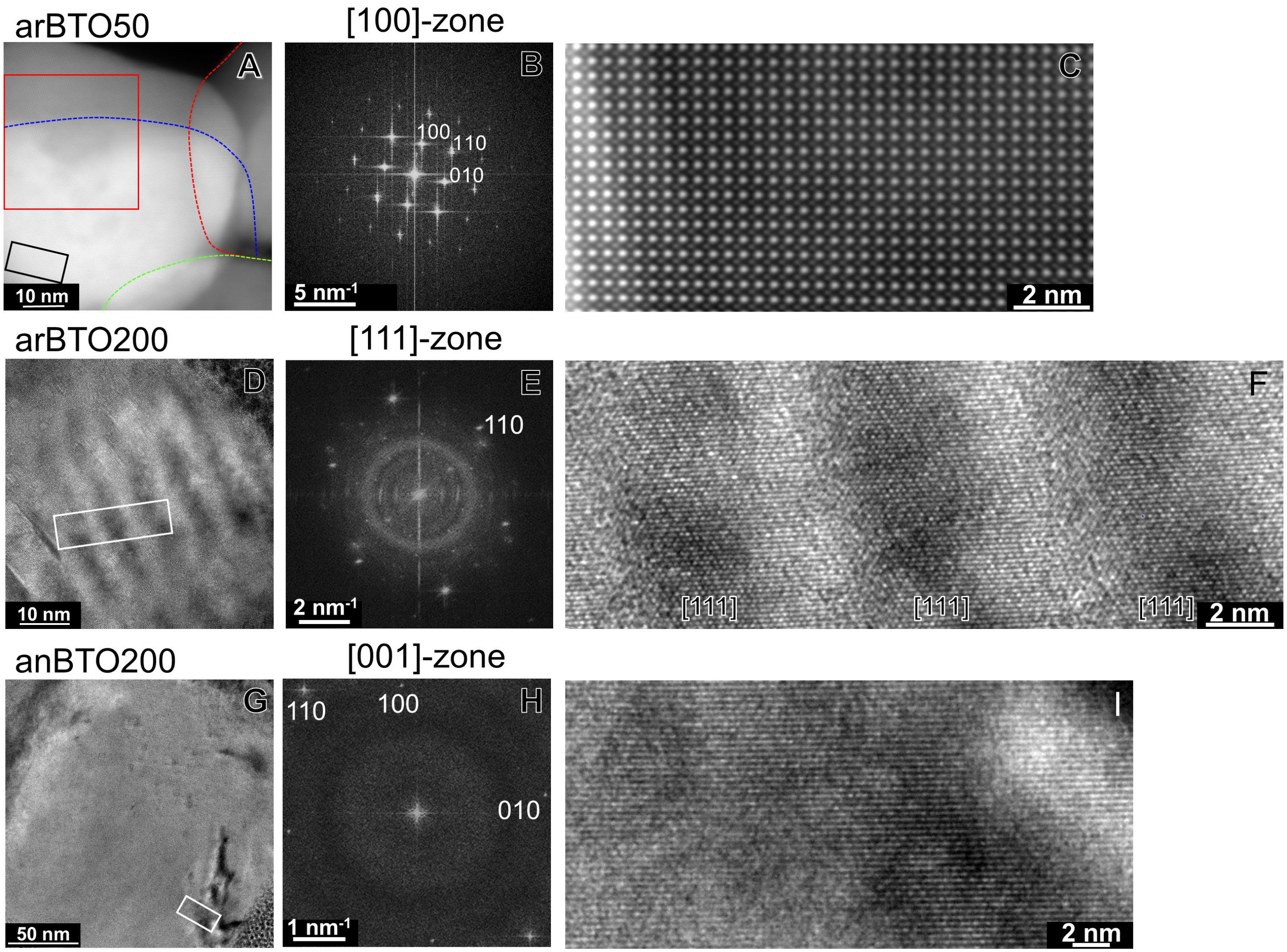

Fig. 6. (A) HAADF STEM micrograph of arBTO50 nanocrystals with (B) FFT pattern of the red square area in (A), and (C) enlarged atomic resolution image from the black rectangular area in (A). (D) Bright-field TEM micrograph of an arBTO200 nanocrystal with (D) FFT pattern of (D) and (E) enlarged image from the white rectangular area in (D). (G) Bright-field TEM micrograph of an anBTO200 nanocrystal with (H) FFT pattern of (G) and (I) enlarged image from the white rectangular area in (D).

High-resolution TEM study

In the next step, high-resolution TEM was used to further understand the role of structural defects on the polymorphism and properties of BTO nanocrystals. First, bright-field high-resolution TEM was used to study whether the arBTO and anBTO nanocrystals were single crystalline or polycrystalline. In Fig. 6A, the HAADF image shows a well-oriented arBTO50 nanocrystal. In the picture, a few arBTO50 nanocrystals overlapped, whose contours were highlighted with red, blue, and green dashed lines, respectively. A Fast Fourier Transform (FFT) analysis of the red square area (2048 pixel × 2048 pixel) revealed a single crystalline [100]-diffraction pattern (Fig. 6B). Fig. 6C shows a high-resolution inversed FFT (iFFT) image cropped from Fig. S19D, corresponding to the black square located in the lower left corner of Fig. 6A. The iFFT treatment process is demonstrated in Fig. S19. In this high-resolution image, Ba and Ti columns were identified with Ba as the bright spots and Ti as the dimmer spots within the Ba squares. As shown in Figs. S19D-G, the primary nanocrystal showed uniform unit cell dimensions and crystal orientation throughout the sample, indicating that this arBTO50 should be single crystal. Similar situation was also observed for other arBTO50 nanocrystals; therefore, we consider that small arBTO50 nanocrystals should be single crystalline. After careful examination of the enlarged area in Fig. 6C, most of the Ti columns were shifted from the center of the unit cell, which seemed to be contradictory to the cubic crystal structure. The most probable reason could be that the viewing direction was slightly tilted from the [100]-zone.

Fig. 6D shows the bright-field TEM micrograph of an arBTO200 nanocrystal prepared by the FIB-cutting technique. In the nanocrystal, alternating bright and dark stripes with an average width of 7.0 nm were observed. The FFT of the nanocrystal showed more than one set of diffraction patterns with the main one close to the [111]-zone of the T_{CF} structure (Fig. 6E). The diffuse ring at a lower angle was from the e-beam deposited Pt NPs on the arBTO200 nanocrystal surface (see the upper-right corner of Fig. 6D). The magnified TEM micrograph from the rectangular area in Fig. 6D showed that the dark stripe had a hexagonal arrangement of the Ba columns along the [111]-zone and the hexagonal pattern vanished in the bright stripes. As seen in the magnified image (Fig. S20), the (110)-spacings of 2.82 Å were unchanged in both dark and bright stripes, indicating that the [111] direction tilted away along the (110) planes for the bright stripes. Meanwhile, the boundaries between two crystalline grains were diffuse, roughly separated by red dash lines in Fig. S20. This experimental observation indicates that this arBTO200 nanocrystal were polycrystalline. It is likely that the as-synthesized arBTO nanocrystals with sizes between 200 and 500 nm were polycrystalline, which limited the ferroelectric domain sizes.

Different from the arBTO200 nanocrystal in Fig. 6D, only one set of [100]-diffraction spots were observed in the FFT pattern (Fig. 6H) of the bright-field TEM image of an anBTO200 nanocrystal (Fig. 6G). Again, the thin section of anBTO200 was prepared by the FIB-cutting technique. Continuous lattice fringes with uniform orientation were seen in the magnified TEM image (Fig. 6I) from the marked rectangular area in Fig. 6G. These fringes were observed throughout the entire anBTO200 nanocrystal with the same spacing and orientation, suggesting that this anBTO200 nanocrystal should be single crystalline. It is likely that the 950 °C thermal annealing had eliminated most grain boundaries and produced more or less single crystalline nanocrystals for anBTO200.

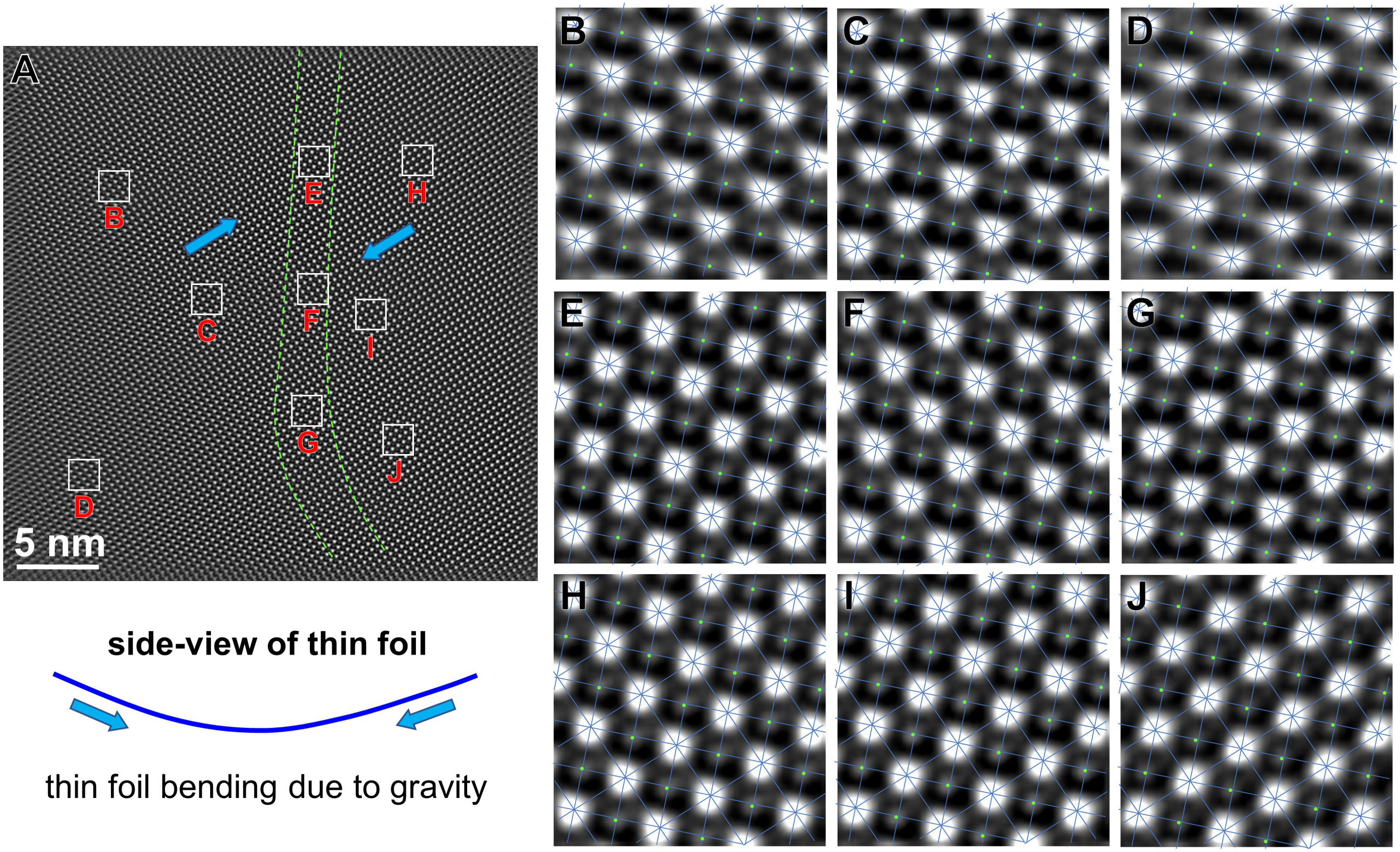

Fig. 7. (A) An iFFT image of an anBTO200 nanocrystal and (B-J) enlarged atomic resolution images of selected areas in (A).

In order to study ferroelectric domain and domain wall structures, atomic resolution HAADF micrographs of arBTO200 and anBTO200 are presented in Figs. S21A,C. The insets show their FFT patterns, respectively. After masking the FFT patterns, Figs. S21B,D show corresponding iFFT images. A detailed image analysis was performed on the anBTO200 nanocrystal, and the results are presented in Fig. 7. On the left side of the image in Fig. 7A, Ti shifted in the upright direction from the center of the Ba squares, and three example areas are shown in Figs. 7B,C,D. It seemed that the dipole moment was along the upright direction for the left half of the image in Fig. 7A. For a narrow band between two green dashed lines, Ti located almost in center of the Ba squares. Three enlarged areas are shown in Figs. 7E,F,G. On the right side of the image in Fig. 7A, Ti shifted in the down-left direction from the centers of the Ba squares, and three example areas are shown in Figs. 7H,I,J. This suggested an opposite dipole moment with respect to the left part of the image. Because the 180°-domain wall should be parallel to the dipole moment directions, the thin stripe between the green dashed lines in Fig. 7A should not be a 180°-domain wall. Meanwhile, the displacement of the center Ti with respect to the square unit cell of Ba was as large as 5-8%, which is significantly higher than the theoretical 1% displacement [i.e., $(c/a-1)\times100\%$] for tetragonal $BaTiO_3$. Given these TEM results, we consider that the observed Ti-displacement should be caused by the bending of the large thin-foil sample, as shown at the bottom of Fig. 7A. The bending could likely happen during the FIB-thinning process by the high-energy ion beam or due to the gravity effect. Similar situation was also observed for arBTO200, as shown in Fig. S22. Such a phenomenon should not happen for BTO nanocrystals smaller than 50 nm, because the size of the BTO nanocrystals is small enough to be directly observed in TEM. Therefore, this FIB-cutting method to prepare thin-section samples for high-resolution TEM study was not suitable for the study of ferroelectric domains and domain walls for 200-500 nm BTO nanocrystals. In the future, better sample preparation methods should be developed to study domain and domain wall structures in BTO nanocrystals with a size of several hundred nanometers.

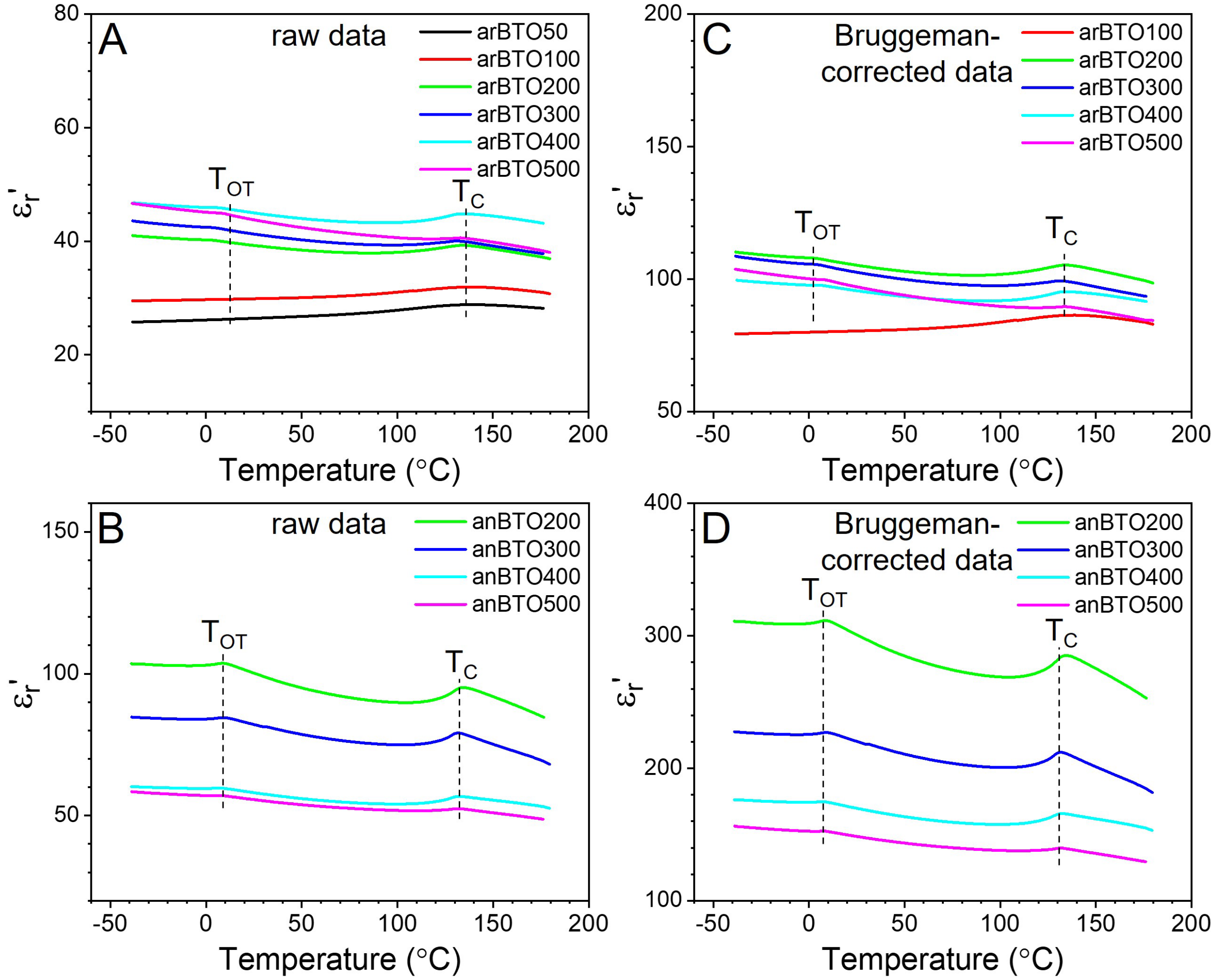

Fig. 8. Temperature-scan real part of the relative permittivity (ε_r') at 1 kHz for the hydraulic-pressed BTO-silicone rubber composites containing (A) arBTO50-arBTO500 and (B) anBTO200-anBTO500 nanocrystals. The calculated ε_r' for (C) arBTO100-arBTO500 and (D) anBTO200-anBTO500 nanocrystals using the Bruggeman equation.

Dielectric properties studied by BDS

Currently, it is not possible to accurately measure the linear dielectric properties of a single BTO nanocrystal. First, it is difficult to implement the parallel plate capacitor sample geometry for nanocrystals. To prepare viable capacitor samples, chemical vapor deposition has been used to prepare a thin BTO film, sandwiched by two conductive layers.[49, 50] Then, FIB is used to cut the continuous film into nanosized parallel-plate samples. Second, it is demonstrated that the stray capacitance from the atomic force microscope is significantly higher than the sample capacitance.[49] It is difficult to determine the stray capacitance and then accurately subtract it for the BDS measurements.

Instead, a slurry[51] or polymer composite[6, 21] approach should be used. In this approach, the dielectric constant of the slurry or polymer composite is measured. The dielectric constant of the nanoparticles is obtained via either a simulation method or the mixing rules. Among various mixing rules, only Maxwell-Garnett and Bruggeman mixing rules use explicit physical models to predict the composite dielectric constants.[6] All other mixing rules are just mathematical fitting of the experimental data. Both Maxwell-Garnett and Bruggeman mixing rules are developed for dilute composites with the fact that Bruggeman model considers the particle-particle dipolar interactions and Maxwell-Garnett does not. As a result, the Maxwell-Garnett mixing rule predicts a lower dielectric constant of the composite than the Bruggeman mixing rule. From prior experimental studies, the Bruggeman prediction matches the experimental results better than the Maxwell-Garnett prediction.[6, 21-23] For the simulation approach, various methods have been used, including finite element model (FEM),[46] Monte Carlo FEM,[52] finite difference quasielectrostatic modeling,[53] phase-field simulation,[54] and equivalent capacitance model.[55] For most commercial FEM packages, the particle-particle dipolar interaction is often ignored;[46] therefore, the dielectric constant of the composites from commercial FEM is usually underestimated, like the Maxwell-Garnett mixing rule.

In our recent coarse-grained molecular dynamics (MD) simulations of polymer nanocomposites, the particle-particle dipolar interactions are specifically considered.[56, 57] At relatively high filler contents (i.e., 40-60 vol.%), the Bruggeman prediction matches the MD simulation results, and both could fit experimental results reasonably well. Note, at a low filler content (i.e., <30 vol.%), the Bruggeman prediction is lower than the MD simulation and experimental results. An example is shown for the polypropylene (PP)/BTO70 (70 nm BTO particles) nanocomposites in Fig. S23A.[21] Only for the PP/BTO70-0.30 nanocomposite, meaningful solution could be obtained with the BTO70 dielectric constant slightly lower than 100.

In this work, hydraulic-pressed BTO pellets with 20 vol.% (i.e., 4.3 wt.% of the composite) silicone rubber were used for the BDS study. There are several considerations for choosing this sample preparation method. First, silicone rubber was used as the binder to hold the BTO nanoparticles together. If no polymer binder was used, the compressed pellets were easy to break into pieces when handled with tweezers (over 90% chances). With the silicone rubber binder, the failure rate substantially decreased below 20%. Second, the compressed BTO pellets with a particle packing fraction around 55% would contain a significant amount of interstitial void among randomly packed or jammed particles. One concern for the interstitial void was the chance for enhanced ion conduction and subsequent Maxwell-Wagner-Sillars (MWS) interfacial polarization,[58] which would significantly increase both the real (ε_r') and imaginary (ε_r'') parts of the relative permittivity and the intrinsic permittivity of the nanocomposites would be over-estimated. Therefore, it might be better to use polymer nanocomposites without any void, because the insulating polymer matrix would stop ionic conduction. It is known that the percolation threshold for nanocomposites with spherical particles is around 35 vol.%.[53] Above this percolation threshold, void could be somewhat inevitable due to particle jamming. In a previous work, we prepared void-free PP/BTO70 nanocomposites with the volume fraction below 35 vol.%.[21] Surprisingly, frequency-scan BDS results still exhibited the ionic MWS interfacial polarization at low frequencies, especially at high temperatures. We consider that the interface between the PP matrix and the BTO particles might still contain a small gap due to poor compatibility, which could enable the impurity ion conduction in the interstitial space of the "void-free" nanocomposites. In addition, we still had the problem that Bruggeman equation would not work for nanocomposites with packing fraction below 30%. Therefore, we should not use the void-free nanocomposites with packing fraction below 35% to extract the intrinsic dielectric constant for BTO particles.

The quality of the compressed BTO pellets was examined by SEM. Example micrographs of anBTO pellets before and after gold sputtering are shown in Fig. S24. As we can see, the anBTO particles were densely packed with nanosized interstitial voids. During sputtering, the gold crystals quickly filled up the interstitial nano-voids and did not have a chance to penetrate deeply into the pellets. Therefore, a good metal-insulator-metal capacitor was achieved for the BDS study. Example frequency-scan BDS results for the compressed arBTO300 and arBTO500 at room temperature are shown in Fig. S25. Again, the effect of absorbed moisture was clearly seen. The fresh compressed BTO pellets, which had absorbed moisture, showed significant ionic MWS interfacial polarization. After thermal annealing at 110 °C for 30 min in the Novocontrol sample chamber with a dry nitrogen atmosphere, the MWS interfacial polarization was substantially suppressed. The ε_r' plots showed nearly flat curves for high frequencies between 1 kHz and 1 MHz. Meanwhile, the dissipation factor ($\tan\delta$) at 1 kHz was as low as 0.005. Therefore, in this study we used the 1 kHz ε_r' data as the dielectric constant of the nanocomposite to extract the intrinsic dielectric constant of BTO particles using the Bruggeman mixing rule.

For the BDS measurements, the packing fraction of the BTO pellets was an important factor for the Bruggeman-corrected dielectric constant. As shown for the BTO50 pellets in Figs. S23B and C, different packing fractions would lead to different calculated dielectric constants for the BTO50 particles. In general, the lower the packing fraction, the higher Bruggeman-corrected dielectric constant of the BTO particles. To minimize the effect of packing fraction, we chose the packing fraction above 52% for this study. Because the BTO50 nanoparticles had more or less a donut shape, the packing fraction was often lower than 50%. Therefore, we will not use the Bruggeman mixing rule to calculate the BTO50 dielectric constant in this study. In addition, another experimental error should originate from the sample thickness. During the IR-pressing, we rotated the metal rod every 90° followed by compression for many times to make sure the parallelism of both top and bottom surfaces of the pellet. However, there was still 5-7% error in the thickness over the 1 cm^2 area. Taking into account of all sources of errors, we consider that the overall error in the BDS measurement of the nanocomposite dielectric constants should be about 10%.

The temperature-scan ε_r' at 1 kHz for the arBTO- and anBTO-silicone rubber composites are presented in Figs. 8A,C, respectively. The complete temperature-scan BDS results, including ε_r', ε_r'', and tanδ under different frequencies are shown in Figs. S26 and S27. From these BDS results, the T_C was not frequency dependent, indicating again the first-order Curie transition. Two ferroelectric transitions were observed for arBTO200-arBTO500 and anBTO200-anBTO500 in Fig. 8: the T_{OT} was 4-9 °C (which was lower than those in DSC) and T_C was 132-134 °C (which was higher than those in DSC). On the other hand, the temperature-dependent ε_r' of arBTO50 and arBTO100 did not exhibited the OT transition. Instead, a broad and weak Curie-like transition was observed around 145 °C at 1 kHz (i.e., similar to the DSC result), which could be attributed to weakening of the tetragonal-fluctuation in the C′$_{TF}$ phase. Moreover, the ε_r' of the C′$_{TF}$ arBTO50 and arBTO100 nanocrystals had a positive temperature dependence, whereas ferroelectric arBTO200-arBTO500 and anBTO200-anBTO500 exhibited a negative temperature dependence. Supposedly, increasing temperature would decrease the dielectric constant due to thermal fluctuation, and this is exactly seen for 200-500 nm arBTO and anBTO nanocrystals. For arBTO50 and arBTO100, we speculate that the frozen tetragonal fluctuations become increasingly mobile and thus increase the dielectric constant upon increasing temperature.

In Fig. 8A, the ε_r' of the composites with ferroelectric arBTO200-arBTO500 nanocrystals were higher than those with paraelectric arBTO50 and arBTO100 nanocrystals. Meanwhile, the ε_r' values generally increased with increasing the particle size. The permittivity of the BTO nanocrystals could be extracted from the composite permittivity using the Bruggeman mixing rule. Based on the measured density of the hydraulic-pressed BTO-silicone rubber pellets, the density of BTO (6.02 g/cm^3), the density of silicone rubber (1.07 g/cm^3), and 4.3 wt.% of the rubber content, the volumetric packing fractions of arBTO nanocrystals were calculated to be 53.4%, 52.1%, 58.8%, 63.4% and 62.1%, and the volume fractions of the silicone rubber were 13.4%, 13.5%, 14.6%, 15.9% and 15.5% for arBTO100, arBTO200, arBTO300, arBTO400, and arBTO500, respectively, in the composite pellets. This indicates that the BTO/rubber composites contained three phases: BTO nanocrystals, silicone rubber, and void. The Bruggeman equation is given by:

$$\eta\frac{\varepsilon_{\mathrm{BTO}}-\varepsilon_c}{\varepsilon_{\mathrm{BTO}}+2\varepsilon_c}+(1-\eta)\frac{\varepsilon_1-\varepsilon_c}{\varepsilon_1+2\varepsilon_c}=0 \qquad (2)$$

where η is the volume fraction of BTO nanocrystals, and ε_c, ε_{BTO}, and ε_1 are the dielectric constants of BTO-silicone rubber composites, BTO nanocrystals, and the mixed phase of silicone rubber and void ($\varepsilon_{air} = 1$, $\varepsilon_{rubber} = 3$), respectively. Because BTO-silicone rubber composite contained three components (BTO nanocrystals, silicone rubber, and void), the Bruggeman approximation was used firstly to calculate the dielectric constant of a mixed phase of silicone rubber and void. Then, it was used again to estimate the dielectric constant of BTO nanocrystals. The extracted ε_r' for the arBTO nanocrystals are shown in Fig. 8C. The ε_r' values of the arBTO50-arBTO500 nanocrystals at 25 °C were calculated to be 86-105 at 1 kHz (Table 1).

Temperature-dependent ε_r' for BTO-silicone rubber composites with anBTO200-anBTO500 were higher as compared to those with arBTO nanocrystals (Fig. 8B). The Bruggeman-corrected ε_r' for anBTO200-anBTO500 are shown in Fig. 8D. The volumetric packing fractions of anBTO200, anBTO300, anBTO400 and anBTO500 were calculated to be 55.0%, 57.5%, 55.2% and 57.3%, and the volume fractions of the silicone rubber were calculated to be 13.8%, 14.4%, 13.8% and 14.3%, respectively, in the composite pellets. At 1 kHz and 25 °C, the Bruggeman ε_r' for the arBTO200-anBTO500 nanocrystals decreased from 301 to 220, 170, and 149 (Table 1). The decrease of ε_r' with increasing the anBTO particle size could be explained as the following. Although anBTO200-anBTO500 were largely single crystalline, they should contain more than one ferroelectric domains (most likely 180°-domains). The smaller the anBTO nanocrystals, the more domains; therefore, more ferroelectric domains and domain walls in smaller anBTO nanocrystals led to a higher dielectric constant. This is similar to the case for bulk BTO when the grain size decreases down to 1 μm.[8, 9] However, other explanations could also be possible because the exact domain structures could not be identified by high-resolution TEM. Future studies are needed. Note that the highest ε_r' of ~300 at 1 kHz and 25 °C for anBTO200 was significantly lower than the ε_r' (~1800) for sintered $BaTiO_3$ with large grain sizes.[6, 7, 11] Also, it is lower than the ε_r' (~1000) of the multi-domain BTO (001)-SC (Fig. S28), and was similar to that (~270) for a single-domain BTO (001)-SC reported in the literature.[59, 60] This can be largely attributed to the disappearance of 90° domains when the internal strain energy goes to zero for these nanosized single crystals.

Discussion of the main observations from this study

The main observations from this study can be summarized into the following. i) For arBTO ≤ 100 nm, the tetragonal ferroelectric phase disappears and the C'_{TF} phase persists. ii) For arBTO and anBTO ≥ 200 nm, the tetragonal ferroelectric phase becomes macroscopically stable; however, their dielectric constants (<300) are much lower than those (a few thousands) of the bulk BTO. iii) Thermal annealing reduces defects (e.g., point defects, dislocations, and grain boundary) and enlarges the particle size for the anBTO particles. Consequently, their dielectric constants are higher than those of arBTO particles. It is imperative to provide a plausible explanation for these observations.

From the Williamson-Hall analysis results in Table 1, small BTO nanoparticles (≤ 100 nm) have microstrain values nearly 10 times those of large BTO particles (≥ 200 nm). This clearly indicates that small BTO nanoparticles contain more structural defects, which should be present on the particle surface and/or in the bulk. For ferroelectric anBTO particles, they are more or less single crystals. Because of the lack of the internal strain energy, 90° domains should not exist in these nanosized single crystals, and only 180° domains may be present. As a result, the dipolar polarization becomes weak, and low dielectric constants of 150-300 are resulted primarily from the intrinsic ionic polarization. For example, paraelectric $SrTiO_3$ has a similar dielectric constant of 300 at room temperature because of the ionic polarization.[8, 9] Finally, thermal annealing of the arBTO particles at high temperatures reduces structural defects, resulting in larger crystalline grain and ferroelectric domain sizes for the anBTO particles. As a result of larger ferroelectric domains, the anBTO particles exhibit higher dielectric constants than the arBTO particles.

At this moment, we could not determine which defect, surface or bulk one, dominates the formation of paraelectric BTO particles with the $\mathrm{C}'_{\mathrm{TF}}$ phase. Meanwhile, the ferroelectric domain and domain wall structures have not been identified for 200-600 nm ferroelectric BTO particles. These are largely attributed to the difficulty in preparing good thin-section samples from large-sized BTO particles for high-resolution TEM study. In the future, new experimental techniques should be developed to tackle this problem.

Conclusions

In summary, we performed a systematic investigation into the crystal structure-dielectric property correlation of combustion-synthesized arBTO nanocrystals and thermally annealed anBTO nanocrystals. The size effect for $BaTiO_3$ nanocrystals seemed not that simple, and the contradictory phase assignment from XRD and Raman was resolved. First, arBTO50 and arBTO100 exhibited the $\mathrm{C}'_{\mathrm{TF}}$ phase (detected by XRD) with static tetragonal fluctuations (detected by Raman). The Williamson-Hall analysis indicated that arBTO50 and arBTO100 contained more structural defects because their microstrain values were about 10 times higher than those for ferroelectric arBTO and anBTO particles. Second, 200-500 nm arBTO and anBTO nanocrystals exhibited the T_{CF} phase with a small content (7-13%) of cubic fraction, as revealed by the Rietveld fitting. These results suggested that surface and bulk defects in BTO nanocrystals should have played an important role in their crystal structures.

From the high-resolution TEM study, small arBTO nanocrystals, such as arBTO50, were single crystalline. The as-synthesized arBTO200 contained multiple crystalline grains; however, the anBTO200 became more or less single crystalline, due to the elimination of grain boundaries by thermal annealing at 950 °C. To study the domain structures, the FIB-cutting method was used for BTO nanocrystals above 100 nm. However, due to the bending of thin sample sections, detailed domain structures and domain walls could not be successfully unraveled by TEM. Therefore, it was difficult to pinpoint these structural defects in the BTO nanocrystals.

Because of crystal perfection from 950 °C-annealing, anBTO nanocrystals manifested significantly increased ΔH_C (up to 1.06 J/g) compared to arBTO nanocrystals, indicating the growth of large ferroelectric domains. Meanwhile, their dielectric constant substantially increased from ~100 for multi-grain arBTO to 150-300 for single-grain anBTO around room temperature. However, this dielectric constant is still much lower than that (~1000) of the multi-domain BTO (001)-SC. The understanding obtained from this study can help us design new high-κ and low loss nanomaterials (e.g., relaxor ferroelectric nanocrystals) for next-generation multilayer ceramic capacitors.

Acknowledgements

L.Z. and Z.L. acknowledges the financial support from the NSF Division of Materials Research (DMR-1709420). The XRD study used the 11-BM CMS beamline of National Synchrotron Light Source II (NSLS-II), Brookhaven National Laboratory (BNL), a U.S. Department of Energy (DOE) User Facility operated for the Office of Science by BNL under contract DE-SC0012704. Dr. Robert E. A. Williams performed electron microscopy at the Center for Electron Microscopy and Analysis at the Ohio State University. Part of FIB and TEM analysis were conducted at the Center for Nanophase Materials Sciences, Oak Ridge National Laboratory (ORNL), which is a DOE Office of Science User Facility. The authors thank Dorothy Coffey at

ORNL for FIB experiments and Xiang Cheng at Case Western Reserve University for the FTIR experiments.

CRediT author statement

Qiong Li: Data curation, Formal analysis, Investigation, Methodology, Validation, Visualization, Writing – Original Draft, Writing – Review & Editing; Tianxiong Ju: Data curation, Formal analysis, Investigation, Methodology, Validation, Visualization; Ruipeng Li: Data curation, Formal analysis, Investigation; Shuang Wang: Investigation, Methodology, Validation, Visualization; Yongfang Yang: Conceptualization, Methodology, Supervision, Validation; Hatsuo Ishida: Data curation, Formal analysis, Investigation, Methodology, Writing – review and editing; Yeu-Wei Harn: Data curation, Formal analysis, Investigation, Methodology; Jihua Chen: Data curation, Formal analysis, Investigation, Methodology, Visualization; Benjamin Hirt: Formal analysis, Investigation, Methodology, Validation; Alp Sehirlioglu: Methodology, Supervision, Writing – review and editing; Zhiqun Lin: Conceptualization, Funding acquisition, Project administration, Supervision, Writing – review and editing; Lei Zhu: Conceptualization, Funding acquisition, Project administration, Supervision, Validation, Writing – original draft, Writing – review and editing

References

1. H. Kishi, Y. Mizuno and H. Chazono, *Jpn. J. Appl. Phys.*, 2003, **42**, 1-15.
2. M. J. Pan and C. A. Randall, *IEEE Electr. Insul. Mag.*, 2010, **26**, 44-50.
3. K. Hong, T. H. Lee, J. M. Suh, S. H. Yoon and H. W. Jang, *J. Mater. Chem. C*, 2019, **7**, 9782-9802.

4. M. Feng, Y. Feng, T. Zhang, J. Li, Q. Chen, Q. Chi and Q. Lei, *Adv. Sci.*, 2021, **8**, 2102221.
5. C. Pithan, D. Hennings and R. Waser, *Int. J. Appl. Ceram. Technol.*, 2005, **2**, 1-14.
6. G. Zhang, Q. Li, E. Allahyarov, Y. Li and L. Zhu, *ACS Appl. Mater. Interfaces*, 2021, **13**, 37939-37960.
7. V. Buscaglia and C. A. Randall, *J. Eur. Ceram. Soc.*, 2020, **40**, 3744-3758.
8. T. Tsurumi, J. Li, T. Hoshina, H. Kakemoto, M. Nakada and J. Akedo, *Appl. Phys. Lett.*, 2007, **91**, 182905.
9. T. Teranishi, T. Hoshina and T. Tsurumi, *Mater. Sci. Eng. B*, 2009, **161**, 55-60.
10. G. Arlt, D. Hennings and G. Dewith, *J. Appl. Phys.*, 1985, **58**, 1619-1625.
11. T. Hoshina, *J. Ceram. Soc. Jpn.*, 2013, **121**, 156-161.
12. A. K. Goswami, *J. Appl. Phys.*, 1969, **40**, 619-624.
13. H. I. Hsiang and F. S. Yen, *Jpn. J. Appl. Phys.*, 1993, **32**, 5029-5035.
14. B. Jiang, J. Iocozzia, L. Zhao, H. Zhang, Y.-W. Harn, Y. Chen and Z. Lin, *Chem. Soc. Rev.*, 2019, **48**, 1194-1228.
15. P. K. Dutta, R. Asiaie, S. A. Akbar and W. Zhu, *Chem. Mater.*, 1994, **6**, 1542-1548.
16. C. W. Beier, M. A. Cuevas and R. L. Brutchey, *Langmuir*, 2010, **26**, 5067-5071.
17. A. Varma, A. S. Mukasyan, A. S. Rogachev and K. V. Manukyan, *Chem. Rev.*, 2016, **116**, 14493-14586.
18. J. L. Clabel, I. T. Awan, A. H. Pinto, I. C. Nogueira, V. D. N. Bezzon, E. R. Leite, D. T. Balogh, V. R. Mastelaro, S. O. Ferreira and E. Marega, *Ceram. Int.*, 2020, **46**, 2987-3001.
19. S. Siddabattuni, T. P. Schuman, V. Petrovsky and F. Dogan, *J. Am. Ceram. Soc.*, 2013, **96**, 1490-1496.
20. J. Adam, T. Lehnert, G. Klein and R. M. McMeeking, *Nanotechnology*, 2014, **25**, 065704.

21. G. Zhang, D. Brannum, D. Dong, L. Tang, E. Allahyarov, S. Tang, K. Kodweis, J.-K. Lee and L. Zhu, *Chem. Mater.*, 2016, **28**, 4646-4660.

22. H. Z. Guo, Y. Mudryk, M. I. Ahmad, X. C. Pang, L. Zhao, M. Akinc, V. K. Pecharsky, N. Bowler, Z. Q. Lin and X. Tan, *J. Mater. Chem.*, 2012, **22**, 23944-23951.

23. B. Jiang, X. Pang, B. Li and Z. Lin, *J. Am. Chem. Soc.*, 2015, **137**, 11760-11767.

24. S. Kappadan, T. W. Gebreab, S. Thomas and N. Kalarikkal, *Mater. Sci. Semicond. Process.*, 2016, **51**, 42-47.

25. T. Noma, S. Wada, M. Yano and T. Suzuki, *J. Appl. Phys.*, 1996, **80**, 5223-5233.

26. G. Caruntu, R. Rarig, I. Dumitru and C. J. O'Connor, *J. Mater. Chem.*, 2006, **16**, 752-758.

27. P. W. Voorhees, *J. Stat. Phys.*, 1985, **38**, 231-252.

28. A. A. Bush, V. P. Sirotinkin and S. A. Ivanov, *Crystallogr. Rep.*, 2020, **65**, 1025-1032.

29. M. B. Smith, K. Page, T. Siegrist, P. L. Redmond, E. C. Walter, R. Seshadri, L. E. Brus and M. L. Steigerwald, *J. Am. Chem. Soc.*, 2008, **130**, 6955-6963.

30. T. Hoshina, S. Wada, Y. Kuroiwa and T. Tsurumi, *Appl. Phys. Lett.*, 2008, **93**, 192914.

31. R. Asiaie, W. D. Zhu, S. A. Akbar and P. K. Dutta, *Chem. Mater.*, 1996, **8**, 226-234.

32. J. E. Daniels, J. L. Jones and T. R. Finlayson, *J. Phys. D – Appl. Phys.*, 2006, **39**, 5294-5299.

33. G. K. Williamson and W. H. Hall, *Acta Metallurgica*, 1953, **1**, 22-31.

34. M. Khan, A. Mishra, J. Shukla and P. Sharma, AIP Conf. Proc., 2019, **2100**, 020138.

35. H. Hayashi and T. Ebina, *J. Ceram. Soc. Jpn.*, 2018, **126**, 214-220.

36. S. Kumar and V. Luthra, *J. Phys. Chem. Solids*, 2021, **154**, 110079.

37. Y. Shiratori, C. Pithan, J. Dornseiffer and R. Waser, *J. Raman Spectrosc.*, 2007, **38**, 1288-1299.

38. Y. Shiratori, C. Pithan, J. Dornseiffer and R. Waser, *J. Raman Spectrosc.*, 2007, **38**, 1300-1306.

39. A. Bencan, E. Oveisi, S. Hashemizadeh, V. K. Veerapandiyan, T. Hoshina, T. Rojac, M. Deluca, G. Drazic and D. Damjanovic, *Nat. Commun.*, 2021, **12**, 3509.

40. S. Wada, T. Suzuki, M. Osada, M. Kakihana and T. Noma, *Jpn. J. Appl. Phys.*, 1998, **37**, 5385-5393.

41. Z. G. Ye, *Key Eng. Mater.*, 1998, **155-156**, 81-122.

42. A. A. Bokov and Z. G. Ye, *J. Mater. Sci.*, 2006, **41**, 31-52.

43. F. A. Rabuffetti, H. S. Kim, J. A. Enterkin, Y. M. Wang, C. H. Lanier, L. D. Marks, K. R. Poeppelmeier and P. C. Stair, *Chem. Mater.*, 2008, **20**, 5628-5635.

44. N. Sakamoto and T. Hashimoto, *Macromolecules*, 1995, **28**, 6825-6834.

45. N. Sakamoto and T. Hashimoto, *Macromolecules*, 1998, **31**, 3815-3823.

46. S. Wada, T. Hoshina, H. Yasuno, S. M. Nam, H. Kakemoto, T. Tsurumi and M. Yashima, *J. Korean Phys. Soc.*, 2005, **46**, 303-307.

47. I. Spasojevic, G. Sauthier, J. M. Caicedo, A. Verdaguer and N. Domingo, *Appl. Surf. Sci.*, 2021, **565**, 150288.

48. Y. Fujisaki, Y. Shimamoto and Y. Matsui, *Jpn. J. Appl. Phys.*, 1999, **38**, L52-L54.

49. S. Tiedke, T. Schmitz, K. Prume, A. Roelofs, T. Schneller, U. Kall, R. Waser, C. S. Ganpule, V. Nagarajan, A. Stanishevsky and R. Ramesh, *Appl. Phys. Lett.*, 2001, **79**, 3678-3680.

50. A. Rüdiger, T. Schneller, A. Roelofs, S. Tiedke, T. Schmitz and R. Waser, *Appl Phys a-Mater*, 2005, **80**, 1247-1255.

51. S. Wada, H. Yasuno, T. Hoshina, S. M. Nam, H. Kakemoto and T. Tsurumi, *Jpn. J. Appl. Phys.*, 2003, **42**, 6188-6195.
52. R. Guo, J. I. Roscow, C. R. Bowen, H. Luo, Y. J. Huang, Y. P. Ma, K. C. Zhou and D. Zhang, *J. Mater. Chem. A*, 2020, **8**, 3135-3144.
53. J. P. Calame, *J. Appl. Phys.*, 2006, **99**, 084101.
54. X. Zhang, W. W. Chen, J. J. Wang, Y. Shen, L. Gu, Y. H. Lin and C. W. Nan, *Nanoscale*, 2014, **6**, 6701-6709.
55. S. K. Patil, M. Y. Koledintseva, R. W. Schwartz and W. Huebner, *J. Appl. Phys.*, 2008, **104**, 074108.
56. E. Allahyarov, H. Lowen and L. Zhu, *Phys. Chem. Chem. Phys.*, 2016, **18**, 19103-19117.
57. E. Allahyarov, *Adv. Theor. Simul.*, 2020, **3**, 2000005.
58. K.-C. Kao, *Dielectric Phenomena in Solids: with Emphasis on Physical Concepts of Electronic Processes*, Elsevier Academic Press, Boston, 2004.
59. W. J. Merz, *Phys. Rev.*, 1949, **75**, 687-687.
60. W. J. Merz, *Phys. Rev.*, 1949, **76**, 1221-1225.